Synergistic Effects of PdO_x-CuO_x Loadings on Methylmercaptan Sensing of Porous WO_3 Microspheres Prepared by Ultrasonic Spray Pyrolysis

Nantikan Tammanoon[a,b,c], Takumi Iwamoto[d], Taro Ueda[d], Takeo Hyodo[d], Anurat Wisitsoraat[c,e], Chaikarn Liewhiran[a,c,f*], and Yasuhiro Shimizu[d**]

[a]Department of Physics and Materials Science, Faculty of Science, Chiang Mai University, Chiang Mai 50202, Thailand

[b]Graduate School, Chiang Mai University, Chiang Mai 50202, Thailand

[c]Center of Advanced Materials for Printed Electronics and Sensors, Materials Science Research Center, Faculty of Science, Chiang Mai University, Chiang Mai 50200, Thailand

[d]Graduate School of Engineering, Nagasaki University, 1-14 Bunkyo-machi, Nagasaki 852-8521, Japan

[e]National Security and Dual-Use Technology Center, National Science and Technology Development Agency (NSTDA), Klong Luang, Phathum Thani 12120, Thailand

[f]Center of Excellence in Materials Science and Technology, Chiang Mai University, Chiang Mai 50200, Thailand

Tel.: +66-81-408-2324; Fax: +66-53-943-445

* Corresponding author: E-mail: cliewhiran@gmail.com

****** Corresponding author: E-mail: shimizu@nagasaki-u.ac.jp

ABSTRACT GRAPHICS

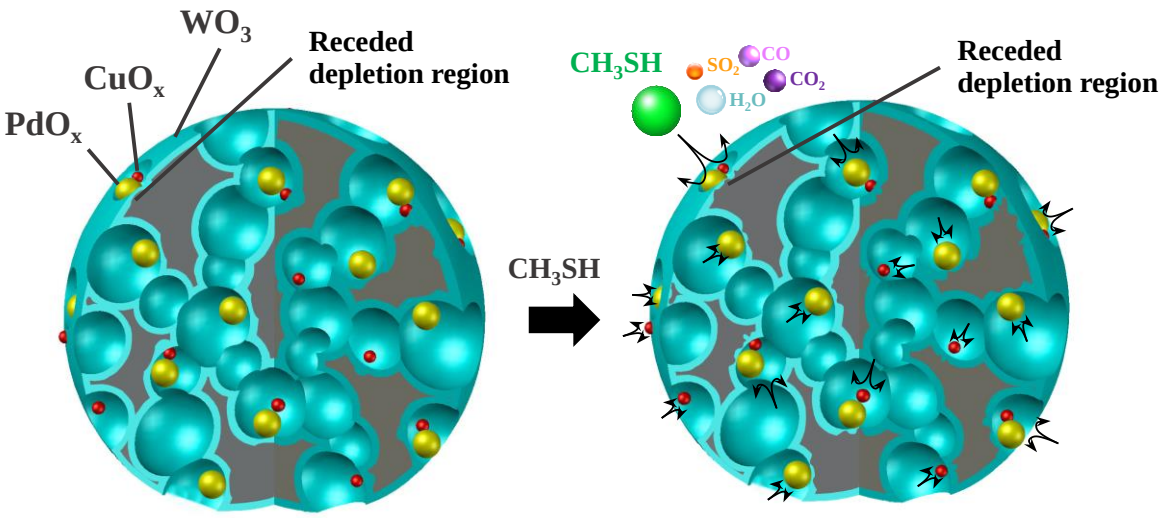

ABSTRACT

In this work, the PdO_x-CuO_x co-loaded porous WO_3 microspheres were synthesized with varying loading levels by ultrasonic-spray pyrolysis (USP) using polymethylmethacrylate (PMMA) microspheres as a vehicle template. The as-prepared sensing materials and their fabricated sensor properties were characterized by X-ray analysis, nitrogen adsorption, and electron microscopy. The gas-sensing properties were studied towards methylmercaptan (CH_3SH), hydrogen sulfide (H_2S), dimethyl sulfide (CH_3SCH_3), nitric oxide (NO), nitrogen dioxide (NO_2), methane (CH_4,), ethanol (C_2H_5OH) and acetone (C_3H_6O) at 0.5 ppm under atmospheric conditions with different operating temperatures ranging from 100–400°C. The results showed that the CH_3SH response of USP-made WO_3 microspheres were collaboratively enhanced by the creation of pores in the microsphere and co-loading of CuO_x and PdO_x at low operating temperatures (≤ 200°C). More importantly, the CH_3SH selectivity against H_2S was significantly improved and high selectivity against CH_3SCH_3, NO, NO_2, CH_4, C_2H_5OH and CH_3COCH_3 were upheld by the incorporation of PdO_x to CuO_x-loaded WO_3 sensors. Therefore, the co-loading of PdO_x-CuO_x on porous WO_3 structures could be promising strategies to achieve highly selective and sensitive CH_3SH sensors, which would be practically useful for specific applications including biomedical and periodontal diagnoses.

KEYWORDS: WO_3, Co-loading, Copper, Palladium, Ultrasonic spray pyrolysis, Methylmercaptan sensor.

1. INTRODUCTION

A particular attention has been recently focused on an exhaled breath analysis for biomedical applications because some gaseous components can serve as indicators of many physiological parameters, which can diagnose the status of possible diseases. For instance, the patients who suffer from diabetes, lung cancer and halitosis can release acetone, toluene, hydrogen sulfide (H_2S) and methylmercaptan (CH_3SH).[1-2] In particular, CH_3SH, an important volatile organic sulfur compound (VOSC), is a principal indicator of halitosis symptoms caused by periodontitis (gum disease). In the periodontitis patients, large periodontal pockets formed in mouth increase the concentration of CH_3SH in the exhaled breath, which will become higher than that of another key marker, H_2S.[3] The application of gas-sensing devices to analyses of VOSCs in the exhaled breath will allow rapid and non-invasive diagnoses of these diseases. However, their gas-sensing properties need to be improved to sensitively and selectively detect these specific gases at lower temperatures as well as a lower threshold limit value (TLV) before they can be practically used with patients.

Semiconductor oxide-based gas sensors have numerous applications due to their advantages such as low cost, high sensitivity, fast response and simplicity of use. In addition to tin dioxide (SnO_2)[4], tungsten trioxide (WO_3) has been considered as another promising candidate for detections of H_2S, CH_3SH, and hydrogen (H_2) as reported in Table 1. Poongodi et al. synthesized WO_3 nanoflakes array via the template-free facile electrodeposition method, and they demonstrated excellent sensing properties towards H_2S.[5] Lee et al. investigated the sensing properties of ZnO, SnO_2, and WO_3-based materials to detect VOCs and H_2S in exhaled breath, and found that the most suitable materials for detection of H_2S is 0.01 wt% Au-loaded WO_3.[1] Furthermore, Amogelang et al. showed that the nanocrystalline VO_2-WO_3 composites effectively

improved the sensing properties to H_2S.[6] Besides, Kabcum et al. enhanced the sensing properties of WO_3 nanorods loading with PdO_x nanoparticles to H_2 and modifying the microstructure with a distinctive preparation process and the study results demonstrated that 1 wt% Pd-loaded WO_3 exhibited the highest response towards H_2 at the optimal operating temperature of 150°C.[7] Wu et al. compared the H_2-sensing performances of commercial WO_3, mesoporous WO_3 (m-WO_3) and Pd-loaded m-WO_3 at room temperature and confirmed that the mesoporous structure and Pd loading effectively improved the H_2-sensing properties of WO_3.[8] In another work, Ueda et al. investigated the effect of Ru or Pd loading on WO_3 on the detection of CH_3SH at 150°C and concluded that 0.5 wt% Ru-loaded WO_3 was the most suitable CH_3SH-sensing material [9]. Recently, He et al. synthesized flower-like WO_3 microspheres modified with CuO nanoparticles by a two-step hydrothermal method and reported that the optimized WO_3/CuO composites (WO_3:CuO = 7:1 in molar ratio) exhibited large response, excellent selectivity and fast response to ppm-level H_2S at a low operating temperature of 80°C.[10]

According to the literatures, it can be inferred that the gas responses towards these specific gases can be effectively enhanced by functionalization with suitable catalysts, e.g., PdO_x and CuO_x, on highly porous WO_3 structures. Generally, porous metal oxide structures can be synthesized via template-based or template-free techniques. The template-based methods, which include additional temporary template materials during synthesis followed by template removal steps, are considered more effective than template-free approaches due to higher attainable porosity, process controllability, reproducibility, and versatility.[3] Mesoporous nanostructures of metal oxides including SnO_2, In_2O_3, and WO_3 have recently been synthesized via different synthetic routes including sol-gel, impregnation, and ultrasonic spray pyrolysis (USP) using some templates such as silica and polymethyl-methacrylate (PMMA) microspheres [8, 11]. Among

these, USP using PMMA microsphere template is particularly promising since it was demonstrated to yield porous metal oxide materials with large surface area suitable as catalyst supports providing excellent gas-sensing performances.[9, 12-13] Nevertheless, additional improvement is demanded to a lower detection limit and enhance selectivity for advanced applications including breath analysis. Co-loading of two or more catalysts is recently reported to offer superior gas-sensing behaviors for differently prepared metal oxide materials.[14-15] However, the approach has not been applied to porous metal oxide structures synthesized by USP with PMMA template. In this study, we investigated for the first time the synergistic effects of functionalized bimetallic oxide catalysts (CuO_x and $PdO_{x'}$) on the sensing properties of the porous WO_3 structures made by USP with PMMA template. The sensors were tested towards CH_3SH and H_2S, which were two key markers for the periodontitis patients.

Table 1. A comparison of gas-sensing performance of different semiconducting metal oxide materials.

Sensing materials	Synthesis route	morphology	Target gas	Conc.	Response	Temp.	Refs.
WO_3	electrodeposition	nanoflakes	H_2S	10 ppm	85%	300°C	[5]
0.03 wt% Au-doped WO_3	heat-treatment	nanoparticles	H_2S	2 ppm	12.40	300°C	[1]
VO_2-WO_3	ball milling	rod-shaped & hollow-shaped	H_2S	5 ppm	9.1	300°C	[6]
1 wt% Pd-loaded WO_3	precipitation/ Impregnation	nanoparticles & nanorods	H_2	0.5 vol%	7.8×10^5	150°C	[7]
1 wt% Pd-loaded WO_3	hydrothermal	mesoporous	H_2	5000 ppm	11.78	RT	[8]
0.5 wt% Ru-WO_3	precipitation	porous oxide	CH_3SH	0.5 ppm	3.09	200°C	[9]
WO_3/CuO composite	hydrothermal	nanoparticles & flower-like	H_2S	5 ppm	105.14	80°C	[10]
0.2 wt% PdO_x/0.1 wt% CuO_x coloaded-WO_3	Ultrasonic spray pyrolysis	porous oxide	CH_3SH	0.5 ppm	11	200°C	Present work

2. MATERIALS AND METHODS

2.1. Synthesis of Porous Pd-Cu/WO_3 Microspheres

Porous WO_3 microspheres were prepared by USP which was previously established by our group [11-12]. The precursor solution was prepared by dissolving appropriate amounts (0.025 M) of ammonium tungstate pentahydrate ($(NH_4)_{10}W_{12}O_{41}\cdot 5H_2O$), copper (II) nitrate ($Cu(NO_3)_2$), and palladium (II) nitrate ($Pd(NO_3)_2$) in the DI water. Subsequently, home-made PMMA microspheres (mean diameter of PMMA microspheres: ca. 70 nm) were mixed with the precursor solution.[11-12] In a typical preparation procedure, the precursor mixture was set in a plastic container, and the mist was then atomized by an ultrasonic vibrator (Honda Electric Co., Ltd., HM-303N, 2.4 MHz). At that time, only small droplets separated in a glass vessel were fed into an electric furnace at 700°C via air flow. As the mists were momentarily heated in the electric furnace, the evaporation of water and the thermal decomposition of precursors together with PMMA microspheres simultaneously occurred, resulting in the formation of spherical and porous (pr)-WO_3-based oxide powders. The USP-made dense-WO_3 microsphere prepared without PMMA microsphere templates was labeled as d-WO_3 whereas pr-WO_3 microspheres loaded with CuO_x were indicated as *n*Cu/pr-WO_3 (*n*: the loading amount of Cu (wt%)). Moreover, pr-WO_3 co-loaded with PdO_x and CuO_x were denoted as *m*Pd-*0.1*Cu/WO_3 (*m*: the loading amount of Pd (wt%)). The Cu and Pd contents were varied in the range of 0.1–1 wt%.

2.2. Preparation of Sensing Films and Measurement of Their Gas-Sensing Properties

Sensing films were prepared by screen-printing methods. The obtained WO_3-based powders were mixed with an appropriate amount of α-terpineol (generally, powder: α-terpineol = 1: 2 in weight) and then thoroughly ground in a mortar for 30 min to form a homogeneous paste

for screen printing. The resulting paste was screen-printed on an alumina substrate equipped with a pair of interdigitated Pt electrodes to form a sensing film. Finally, the resulting film was calcined at 550°C for 5 h in ambient air for binder removal prior to sensing test. The gas-sensing performances of these sensors were measured towards 0.5 ppm CH_3SH, H_2S, dimethyl sulfide (CH_3SCH_3), nitric oxide (NO), nitrogen dioxide (NO_2), methane (CH_4,), ethanol (C_2H_5OH) and acetone (C_3H_6O) in dry air at operating temperatures ranging from 100 to 400°C. All sensors were exposed to a gas sample for 30 min at each gas concentration and the air flux was then resumed for 30 min. The magnitude of gas response was defined as the ratio (R_a/R_g) of sensor resistance to gas (R_g) balanced in dry air to that in dry air (R_a). The response time (t_{res}) was the time to reach 90% of stabilized resistance signal while the recovery time was the time required to recover 90% of baseline resistance.

2.3. Structural Characterizations

The phase composition and crystallinity of nanopowders were measured by X-ray diffraction (XRD: Shimadzu, JDX-8030) using CuK_α radiation (20 kV, 20 mA) with a sweeping speed of 2°/min. Brunauer–Emmett–Teller (BET) and Barrett-Joyner-Halenda (BJH) analyses were performed to estimate the specific surface area and pore size distribution of these powders using the N_2 adsorption isotherm (Micromeritics Inst. Corp., TriStar 3000). The microstructures and size of the microspheres as well as sensing films were observed using transmission electron microscope (TEM: JEOL JSM-2100Plus), field-emission TEM/scanning TEM (FETEM/STEM: Thermo Scientific TALOS F200X), and scanning electron microscopy (SEM; JEOL Ltd., JSM-7500F). In addition, the elemental composition and oxidation states of powders as well as sensing films were characterized by X-ray photoelectron spectroscopy using AlK_α radiation (XPS,

Kratos Analytical Ltd., ACIS-TLATRA DLD), and the binding energy was calibrated using the C1s level (285.0 eV) from usual organic contaminations.

3. RESULTS AND DISCUSSION

3.1. Crystal Structure and Morphology of the Powders

The phase composition and crystallinity of the as-prepared base WO_3 microspheres and Pd-Cu bimetallic oxide functionalized WO_3 microspheres were evaluated from XRD data as illustrated for pr-WO_3, *0.1*Cu/pr-WO_3 and *0.2*Pd-*0.1*Cu/pr-WO_3 in Fig. 1. The complete XRD data were provided in Fig. S1 (Supporting Information). All the diffraction peaks were in accordance with the orthorhombic WO_3 phase (JCPDS No. 01-089-4480), suggesting high crystallinity of these particles. It demonstrated that all samples exhibited three dominant peaks corresponding to (002), (020), and (200) planes of the WO_3 phase. Nevertheless, the secondary diffraction peaks of CuO_x and PdO_x phases were not observed in these patterns due to very low loading amounts of CuO_x and PdO_x. In spite of the absence of peaks related with CuO_x or PdO_x, CuO_x and PdO_x loadings might affect the crystallite size of WO_3 nanostructures. This effect could be clearly seen from the crystallite size of all samples estimated from Debye-Scherer's equation using full widths at half maximum as reported in the inset of Fig. 1. It revealed that the crystallite size of d-WO_3 was smaller than that of pr-WO_3, dictating that the formation of porous WO_3 structures via the PMMA template led to the decrease of the WO_3 crystallite size from 19.2 to 16.8 nm. In contrast, CuO_x loading with the small Cu content of 0.1 wt% caused the crystallites size to increase from 16.8 to 22.3 nm. However, the crystallite size tended to decrease from 22.3 to 16.4 nm with increasing Cu content from 0.1 to 1 wt%. Moreover, the additional loading of 0.1-1 wt% Pd onto 0.1Cu/pr-WO_3 resulted in the decrease of the WO_3 crystallite size

from 22.3 to 16.0-16.3 nm almost independent of Pd content. The overall results indicated that CuO_x and PdO_x loading led to small reductions of the WO_3 crystallite size. A possible explanation was that the loaded CuO_x and PdO_x nanoparticles on porous WO_3 structures acted as surface grain growth inhibitors.

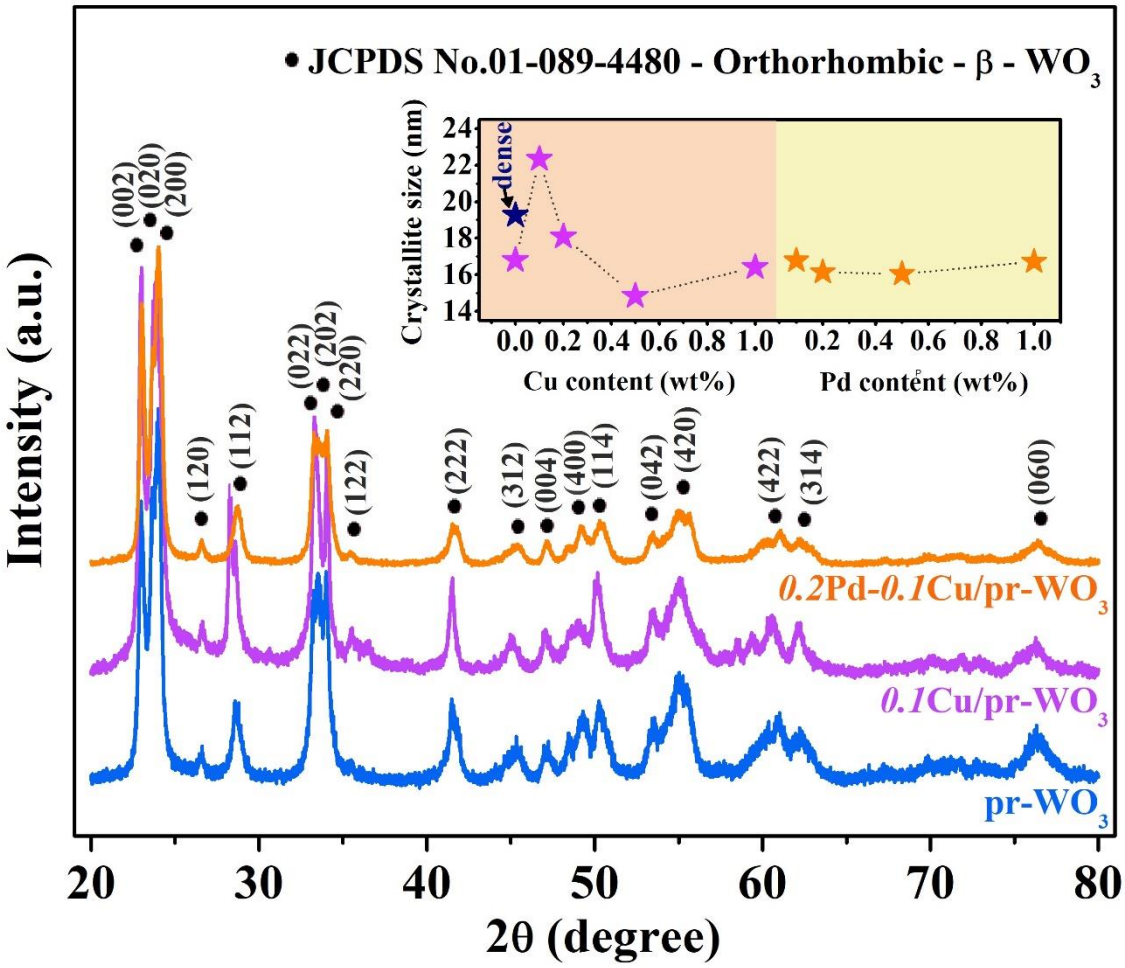

Figure 1. The XRD patterns of pr-WO_3, *0.1*Cu/pr-WO_3 microspheres and *0.2*Pd-*0.1*Cu/WO_3 microspheres. Inset: Crystallite sizes of all materials plotted versus Cu and Pd contents.

The surface chemical compositions and oxidation states of *1*Cu/pr-WO_3 powder and sensor were investigated by XPS as shown in Fig. 2. The full survey spectrum (Fig. 2(a)) confirmed the existence of W4f, Cu2p, O1s, and C1s from typical surface organic contaminations. By omitting the carbon contamination (see the inset table), the Cu contents of

*1*Cu/pr-WO_3 powder and sensor were estimated to be 1.05 and 1.73 wt%, respectively. The value of the powder was close to the value expected from the amount of Cu added to the precursor solution for the UPS process while that of the sensor was considerably higher due possibly to the aggregation of CuO_x on the surface after annealing. The W4f core-level spectrum of powder (Fig. 2(b)) exhibited one doublet pair consisting of $W4f_{7/2}$ and $W4f_{5/2}$ at binding energies of 36.2 eV and 38.3 eV while those of the sensor were slightly shifted to 35.9 eV and 38.0 eV, respectively. Both results could be assigned to the highest oxidation state of W^{6+} for WO_3.[7, 16]

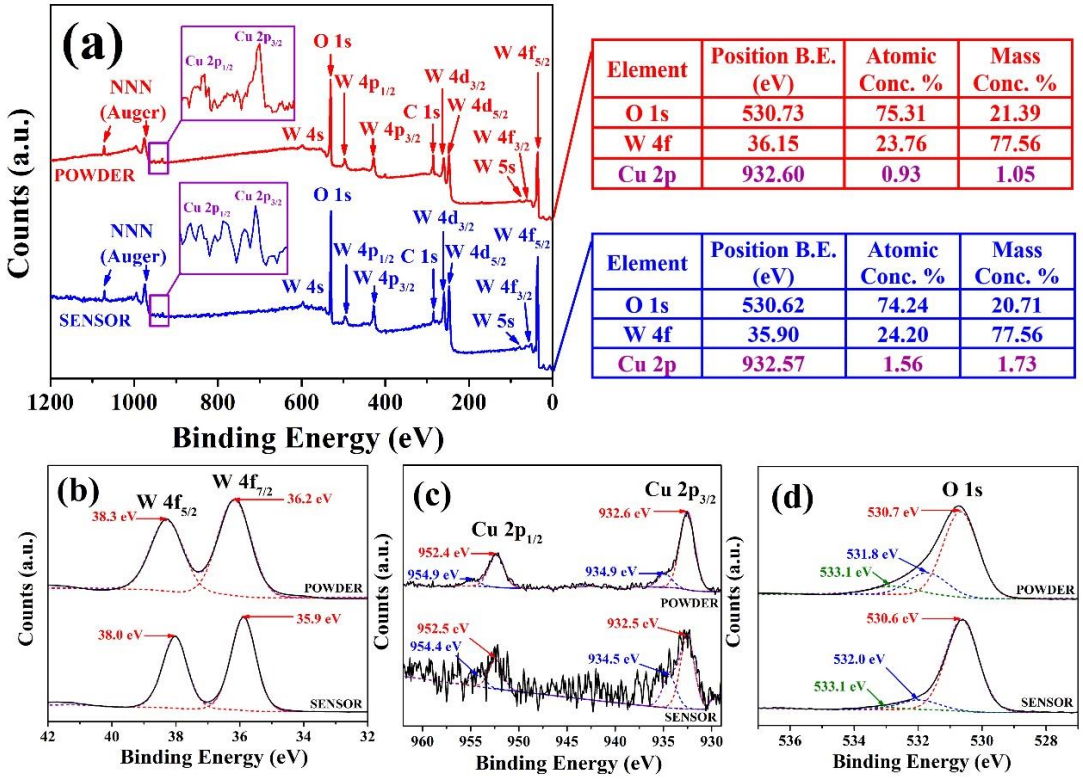

Figure 2. (a) survey, (b) W4f, (c) Cu2p, and (d) O1s XPS spectra of as prepared *1*Cu/pr-WO_3 powder and sensor.

As for the Cu element (Fig. 2(c)), the Cu2p core level of the powder could be decomposed into the main doublet pair, $Cu2p_{3/2}$:$Cu2p_{1/2}$, located at 932.6:952.4 eV and the tiny doublet pair positioned at 934.9:954.9 eV. Similarly, the Cu2p core level of the sensor contained

the major and minor doublet pairs at 932.5:952.5 eV and 934.5 eV:954.4 eV, respectively. The main doublet pair could be ascribed to Cu^{+} of Cu_2O, while the minor doublet pair should be attributed to Cu^{2+} of CuO.[17-18] The contribution of Cu^{2+} for the powder and sensor were found to be 18.7% and 37.3%, respectively. The results indicated that Cu_2O was partially oxidized into CuO after annealing in air at 550°C for 5 h. As for the oxygen element (Fig. 2(d)), the O1s spectrum of the powder could be deconvoluted into three components located at 530.7 (main peak), 531.8 and 533.1 eV while those of the sensor were similarly positioned at 530.6 (main peak), 532.0 and 533.1 eV. The main, secondary and minor peaks could be ascribed to outermost lattice oxygen (O^{2-}) of CuO_x-loaded WO_3 microspheres, chemisorbed oxygen (O_{ads}) and hydroxyl surface groups (OH^{-}) due to water adsorption.[19-20] It also revealed that the contributions of O_{ads} and OH^{-} species were relatively low for the sensor, suggesting that these species were desorbed after the high-temperature annealing in air.

The surface elemental composition and the chemical states of *1*Pd-*0.1*Cu/pr-WO_3 powder and sensor were presented in Fig. 3. The XPS survey scans (Fig. 3(a)) confirmed the presence of W4f, Cu2p, Pd3d, O1s, and C1s in the powder and sensor. By excluding the carbon contamination, the Cu and Pd contents of *1*Pd-*0.1*Cu/pr-WO_3 powder were determined to be 0.16 and 0.53 wt% while those of the sensor were 0.18 and 1.27 wt%, respectively (inset table in Fig. 3(a)). The Fig. 3(b-d) showed the high resolution XPS spectra of W, Cu, and Pd elements. The W4f signals ($W4f_{7/2}$:$W4f_{5/2}$) of the powder and sensor were found at 36.0:38.2 and 35.8:37.9 eV, respectively. The two pairs could also be associated with the highest oxidation state of W^{6+} for WO_3 [16]. For the Cu element, the Cu2p core level of the powder contained a single doublet pair ($Cu2p_{3/2}$:$Cu2p_{1/2}$) positioned at 932.6:952.6 eV corresponding to Cu^{+} of Cu_2O.[18] In the case of sensor, the Cu2p core level comprised one main and one minor doublet components located at

932.5:952.4 eV and 934.8:953.7 eV corresponding to the oxidation states of Cu^{+} and Cu^{2+}, respectively. It revealed that Cu_2O was partially oxidized into CuO (22.7%) after annealing in air at 550 °C. Regarding Pd element, the Pd3d core level of the powder could be divided into the main and minor doublet pairs ($Pd3d_{5/2}$:$Pd3d_{3/2}$) located at 337.7:343.5 eV and 335.8:340.9 eV, respectively. For the sensor, the Pd3d core level exhibited only a single main doublet pair found at 337.3:342.7 eV. The main and minor doublet pairs could be assigned to Pd^{2+} of PdO and Pd^{0} of metal, respectively.[21-22] The results dictated that the metallic Pd species (17.3 %) formed in the powder were mostly oxidized into Pd^{2+} after annealing in air at 550°C for 5 h. Concerning oxygen, the O1s peaks of the *1*Pd-*0.1*Cu/pr-WO_3 powder and sensor also comprised three deconvoluted components (530.5-530.7 eV: O^{2-}, 531.2-531.5 eV: O_{ads} and 532.6-532.9 eV: OH) similar to that of *1*Cu/pr-WO_3. In addition, the contribution of O_{ads} and OH^{-} species were much lower for the sensor indicating that they were largely desorbed after annealing in air similar to the case of *1*Cu/pr-WO_3 powder. Moreover, the *1*Pd-*0.1*Cu/pr-WO_3 powder contained relatively high contents of O_{ads} and OH^{-} in relation to the presence of metallic Pd species.

The SEM micrographs of as-prepared d-WO_3, pr-WO_3, *0.1*Cu/pr-WO_3, and *0.2*Pd-*0.1*Cu/pr-WO_3 microspheres were shown in Fig. 4(a)–(d) with insets of their high-resolution images. Morphologies of all samples were spherical with varying particle sizes in the range of 100–600 nm. In addition, samples prepared with PMMA microspheres exhibited well-developed porous structures due to the thermal decomposition of PMMA microspheres while d-WO_3 displayed solid spherical features with relatively small particle sizes compared with those of other porous samples. Moreover, the morphologies and the particle sizes of porous samples were almost independent of the CuO_x and PdO_x loading. Figure 4(e−h) showed cross-sectional SEM photographs of d-WO_3, pr-WO_3, *0.1*Cu/pr-WO_3, and *0.2*Pd-*0.1*Cu/pr-WO_3 sensing films after

gas-sensing measurements (Fig. 4(e)−(h)). Evidently, all the films were quite homogeneous and the microspheres were connected closely to each other. In addition, there was no significant difference in thickness among these films (12–15 μm) demonstrating the controllability of pasting and screen-printing processes.[9, 11] Therefore, USP and screen printing were demonstrated to be promising for the preparation of practical thick-film metal-oxide gas sensors.

The internal porous structure of pr-WO_3, *1*Cu/pr-WO_3, and *1*Pd-*0.1*Cu/pr-WO_3 microspheres were examined by TEM as shown in Fig. 5. The bright field (BF)-TEM images (Fig. 5 (a), (c), and (e)) demonstrated that the internal structures of the microspheres with diameters of 300–400 nm were mesoporous containing a number of fine nanostructures and pores with dimensions in the range of ~3–30 nm. The inset selected area electron diffraction (SAED) patterns indicated that they were mainly polycrystalline with their diffraction rings corresponding to the (002), (222), and (114) planes of the orthorhombic WO_3 phase in accordance with the XRD data (Fig. 1). The related high-resolution (HR)-TEM images of all samples (Fig. 5 (b), (d), and (f)) illustrated the lattice fringes of crystallites exhibiting d-spacings matched well with various planes of orthorhombic WO_3 phase, confirming high crystallinity of porous WO_3 structures. Moreover, the HR-TEM images of *1*Cu/pr-WO_3 and *1*Pd-*0.1*Cu/pr-WO_3 samples (Fig. 5(e) and (f)) proved the presence of secondary-phase species loaded on WO_3 surfaces. For *1*Cu/pr-WO_3 (Fig. 5(e)), approximately round and oval nanoparticles were widely observed as darker spots marked with blue arrows on the porous WO_3 structures, dictating that Cu_2O or CuO species were loaded on porous WO_3 surface rather than doped into WO_3 lattice.

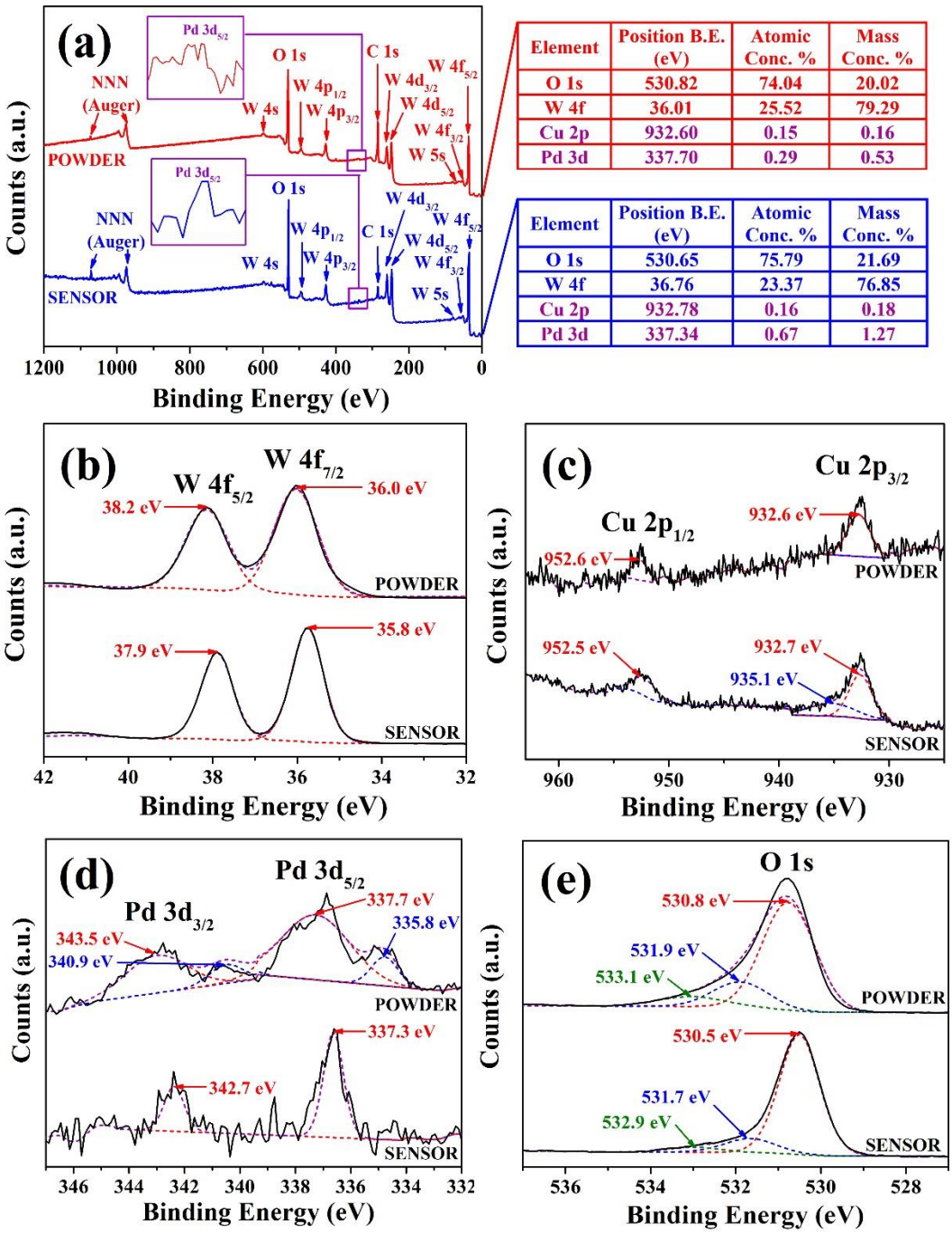

Figure 3. (a) survey, (b) W4f, (c) Cu2p, (d) Pd3d, and (e) O1s XPS spectra of as-prepared *1*Pd-*0.1*Cu/pr-WO_3 powder and sensor.

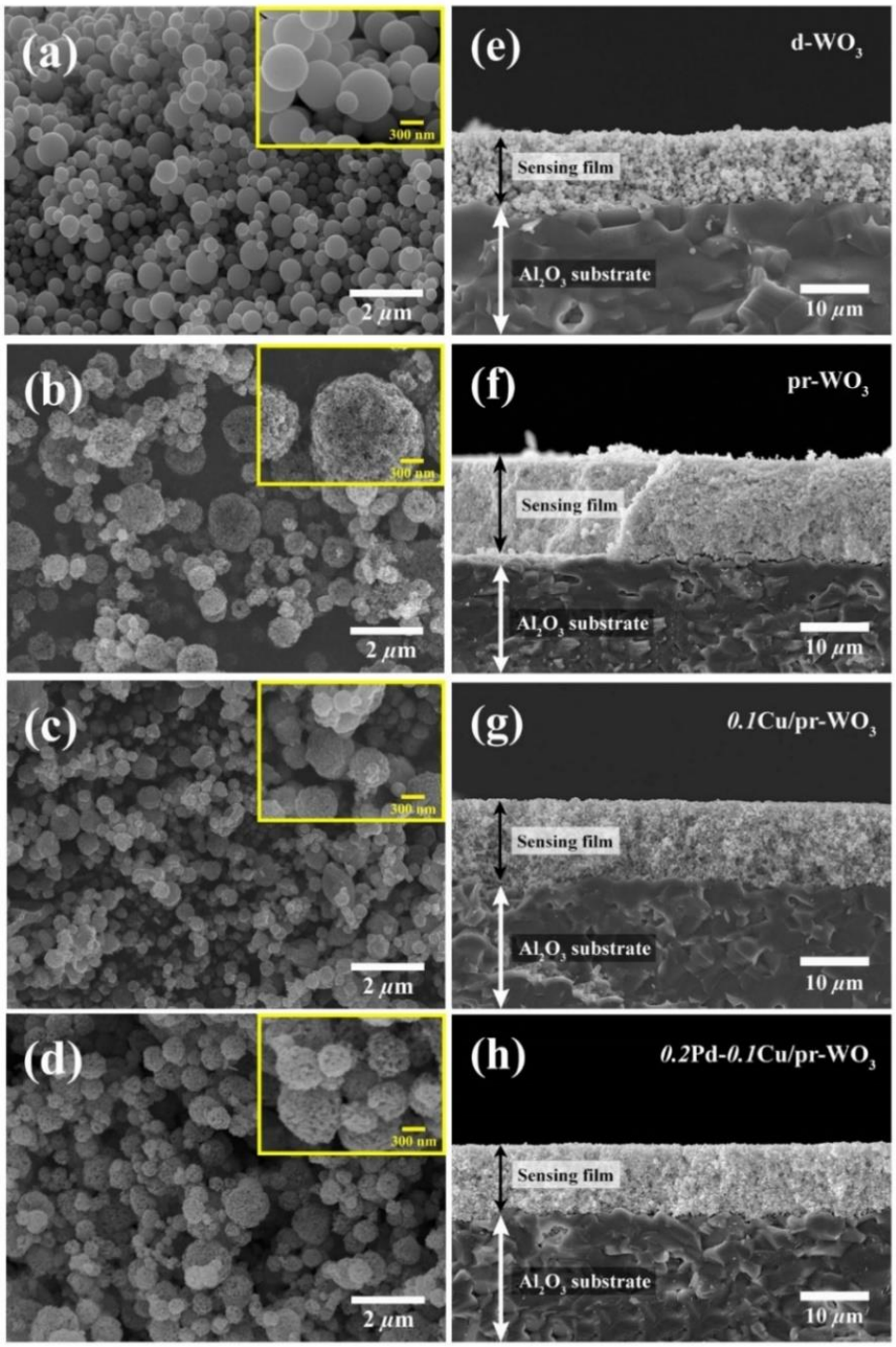

Figure 4. SEM images of as-prepared (a) d-WO_3, (b) pr-WO_3, (c) *0.1*Cu/pr-WO_3, and (d) *0.2*Pd-*0.1*Cu/pr-WO_3 microspheres prepared by USP method, together with insets of their high-resolution images, and cross-sectional SEM images of (e) d-WO_3, (f) pr-WO_3, (g) *0.1*Cu/pr-WO_3, and (h) *0.2*Pd-*0.1*Cu/pr-WO_3 sensors after measuring their gas-sensing properties.

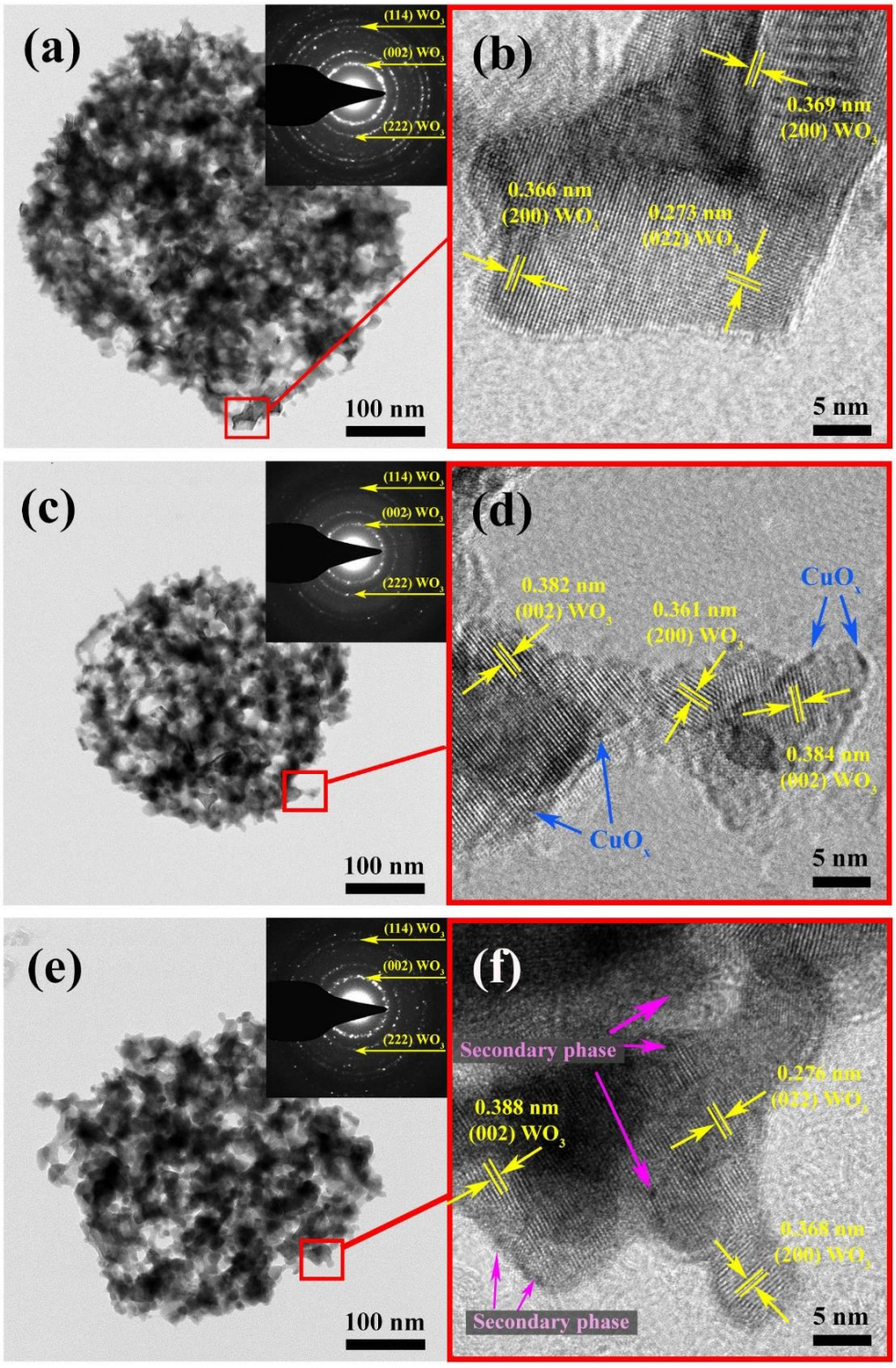

Figure 5. Bright field (BF)-TEM images, selected area electron diffraction (SAED) patterns (inset) and high resolution (HR)-TEM images of (a, b) pr-WO_3, (c, d) *1*Cu/pr-WO_3, and (e, f) *1*Pd-*0.1*Cu/pr-WO_3 microspheres.

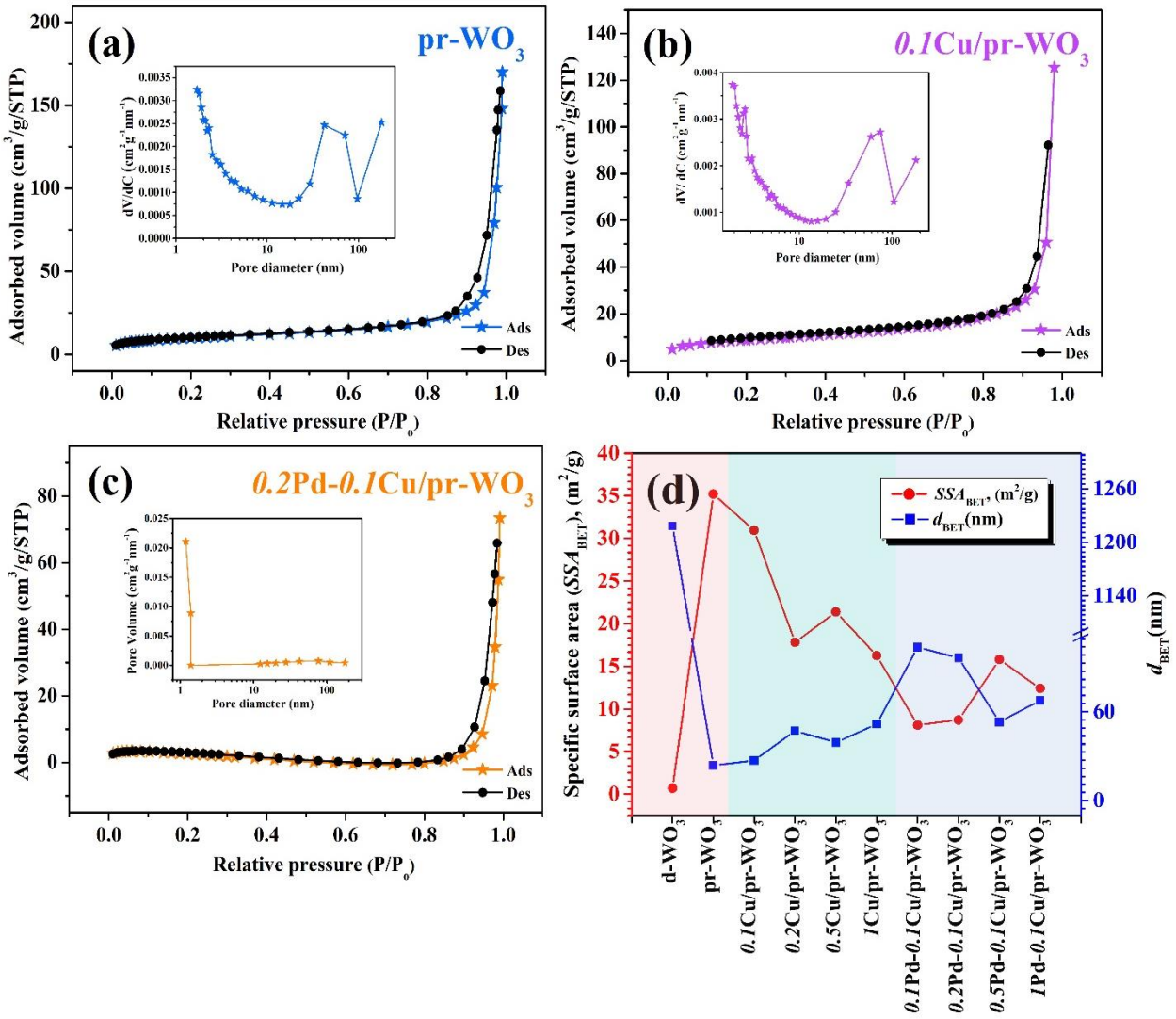

Figure 6. Nitrogen adsorption/desorption isotherms of (a) pr-WO_3, (b) *0.1*Cu/pr-WO_3 and (c) *0.2*Pd-*0.1*Cu/pr-WO_3 together with corresponding BJH pore size distributions (insets), and (d) specific surface area (SSA_{BET}) and average particle diameter (d_{BET}) of all samples.

When considering the Hume–Rothery rule, the ionic radius of host ion (60 pm for W^{6+}) differed from those of loaded Cu species (77 and 73 pm for Cu^{+} and Cu^{2+}, respectively) beyond the relative radii disparity limit of 15%. In addition, the Cu oxidation states of 1+ and 2+ were very different from that of the W oxidation state of 6+. Therefore, the Cu cations could not stably substitute W^{6+} lattice sites resulting in the CuO_x loading on the WO_3 surface. Similarly, the HR-

TEM image of *1*Pd-*0.1*Cu/pr-WO_3 microspheres (Fig. 5(f)) presented some darker spots marked by arrows on the porous WO_3 structures, which could not be definitely assigned to the phase of CuO_x or PdO_x. According to the Hume-Rothery rule, the Pd^{2+} cation also could not substitute the W^{6+} cation due to their large difference of ionic radii (86 vs. 60 pm) and oxidation state (2+ vs. 6+).[21] The results were consistent with all previous studies reporting Pd and/or PdO loading on WO_3 surfaces.

The representative nitrogen sorption isotherms along with corresponding BJH pore-size distributions (insets) were displayed in Figs. 6(a)–(c). The complete isotherm data were included in Fig. S2 (Supporting information). The data revealed that the adsorption profiles of isotherms for all samples were similar but the dense WO_3 sample (d-WO_3) exhibited a wide hysteresis feature distinctive from those of all porous WO_3 samples (pr-WO_3). According to International Union of Pure and Applied Chemistry (IUPAC) classification, this isotherm could be designated as type III corresponding to the unimpeded multilayer adsorption with strong interaction between adsorbates. In addition, the hysteresis loop of d-WO_3 and pr-WO_3 could be matched with type H4 and H3 relating to macro/mesoporous materials with weak capillary condensation in narrow slit-like and slit-shape pores, respectively.[23-24] The narrow slit-like pores could correspond to interparticle voids between solid WO_3 spheres while slit-shape pores were accordingly observed within porous WO_3 spheres as seen in the TEM images (Fig. 5). The corresponding BJH pore-size distributions (insets) provided detailed differences in pore characteristics of the two WO_3 structures. The BJH profile of d-WO_3 (inset of Fig. S2(a)) exhibited only one narrow maxima at ~1 nm while those of pr-WO_3 displayed multi-mode pore size distributions (inset of Figs. 6(a)-(c)) with two main BJH peaks at pore diameters of ~1 and ~40–80 nm. The narrow micropore peaks at ~1 nm of d-WO_3 should correspond to small interparticle gaps among closely packed

solid microsphere and the broad peak at ~1 nm of pr-WO_3 could similarly relate to relatively large short-range interparticle cavities of the porous WO_3 structures. The broad peak at ~40–80 nm should be corresponding to meso/macropores created due to PMMA decomposition since the pore sizes were concordant with the nominal diameter of home-made PMMA microspheres (ca. 70 nm). Furthermore, the peak pore volume related to meso/macropores decreased due to loading with CuO_x as well as PdO_x and the reductions were much higher after PdO_x loading. The BET specific surface area (SSA_{BET}, left axis)) and average BET particle diameter (d_{BET}, right axis) calculated from the isotherm data were reported in Fig. 6(d). It clearly demonstrated that the formation of porous structures using the PMMA template significantly increased SSA_{BET} and reduced d_{BET}. Additionally, the SSA_{BET} tended to decrease while the d_{BET} increased accordingly with increasing Cu and Pd contents. The results might be due to the agglomerations of CuO_x and PdO_x nanoparticles in the pores of pr-WO_3 microspheres. Moreover, the dependencies of d_{BET} on the Cu and Pd contents were similar to those of XRD crystallite size.

3.2. Gas-Sensing Properties

Response transients of pr-WO_3 sensors with varying Cu contents and a d-WO_3 sensor to 0.5 ppm CH_3SH at 200°C in air and the related CH_3SH response together with response and recovery times of these sensors at various operating temperatures (100-400°C) were shown in Fig. 7. When the sensors were exposed to CH_3SH (Fig. 7(a)), their resistances decreased regularly, confirming a typical n-type semiconducting character towards this reducing gas. Among these, the d-WO_3 sensor exhibited the smallest resistance at 200°C in air and relatively small response to CH_3SH at low operating temperatures (100-200°C) as displayed in (Fig. 7(b)). Additionally, the CH_3SH response tended to increase gradually with increasing operating

temperature. On the other hand, the introduction of pore structures into the WO_3 microspheres led to the increased resistance in air over the entire temperature range and enhanced CH_3SH responses at low temperatures (≤ 200°C). In addition, the pr-WO_3 sensor displayed the largest CH_3SH response at 200°C. The loading of CuO_x to the pr-WO_3 microspheres further improved the CH_3SH response at most working temperatures. Among all the sensors, pr-WO_3 sensor loaded with the smallest Cu amount of 0.1 wt% (*0.1*Cu/pr-WO_3) offered the largest CH_3SH response at 200°C. However, the enhancement of CH_3SH response tended to deteriorate with increasing Cu content. Although the *0.2*Cu/pr-WO_3 and *0.5*Cu/pr-WO_3 sensors showed relatively large CH_3SH responses at low temperatures (especially 100°C), the response and recovery times as displayed in Fig. 7(c)-(d) were very poor because the adsorption and desorption rates of CH_3SH were very low due to limited thermal energy, prohibiting practical use of these sensors at these operating conditions. At working temperatures higher than 200°C, the responses of most sensors tended to decline steadily while the response and recovery times inclined to decrease substantially with increasing temperature (Fig. 7(b)-(d)). The results confirmed that the appropriate increase in the operating temperature helped improving the response speed and recovery speed. Thus, the working temperature would be selected by trading off between response and response/recovery times. Overall, CuO_x-loaded porous WO_3 microspheres with the appropriate Cu amount of 0.1 wt% offered the optimal response of 6.5 to 0.5 ppm CH_3SH while attaining moderate response and recovery times at the moderate temperature of 200°C.

Co-loadings with 0.1−1 wt% Pd were applied to further enhance the CH_3SH response of porous WO_3 microspheres with the optimal Cu content of 0.1 wt% (*0.1*Cu/pr-WO_3). The response transients of *0.1*Cu/pr-WO_3 sensors with varying Pd co-loading contents to 0.5 ppm CH_3SH at 200°C in air and the CH_3SH response along with response and recovery times of the

sensors at different operating temperatures were presented in Fig. 8. Fig. 8(a) showed that the co-loading of 0.1 wt% Pd on the *0.1*Cu/pr-WO_3 sensor resulted in a decrease in baseline resistance of the *0.1*Cu/pr-WO_3 sensor but the resistance in air tended to increase with the additional increase of Pd content up to 1 wt%. After exposure to CH_3SH, these sensors also displayed the usual n-type gas-sensing behavior with reductions of resistance. The response characteristics at 200°C were quite similar to those at other operating temperatures (Fig. 8(b)). In addition, the co-loadings of PdO_x and CuO_x were effective in enhancing the CH_3SH response of the *0.1*Cu/pr-WO_3 sensor, particularly at low temperatures (≤ 300°C). However, the responses of most Pd-loaded *0.1*Cu/pr-WO_3 sensors tended to reduce gradually while the response and recovery times inclined to decrease steadily with increasing temperature similar to those with no PdO_x co-loading (Fig. 8(b)-(d)). Thus, Pd-co-loading did not evidently change the temperature-dependent characteristics of CH_3SH sensing parameters. Furthermore, the CH_3SH response of the *0.1*Cu/pr-WO_3 sensor tended to increase with increasing Pd co-loading content from 0 to 0.2 wt% but then inclined to decrease with the additional increase of Pd content up to 1 wt%. In particular, the *0.2*Pd-*0.1*Cu/pr-WO_3 sensor provided the largest response of 8.6 to 0.5 ppm CH_3SH at 200°C. The roles of PdO_x and CuO_x as well as the pore structure to the CH_3SH-sensing properties of WO_3 microspheres would be further discussed in the next section.

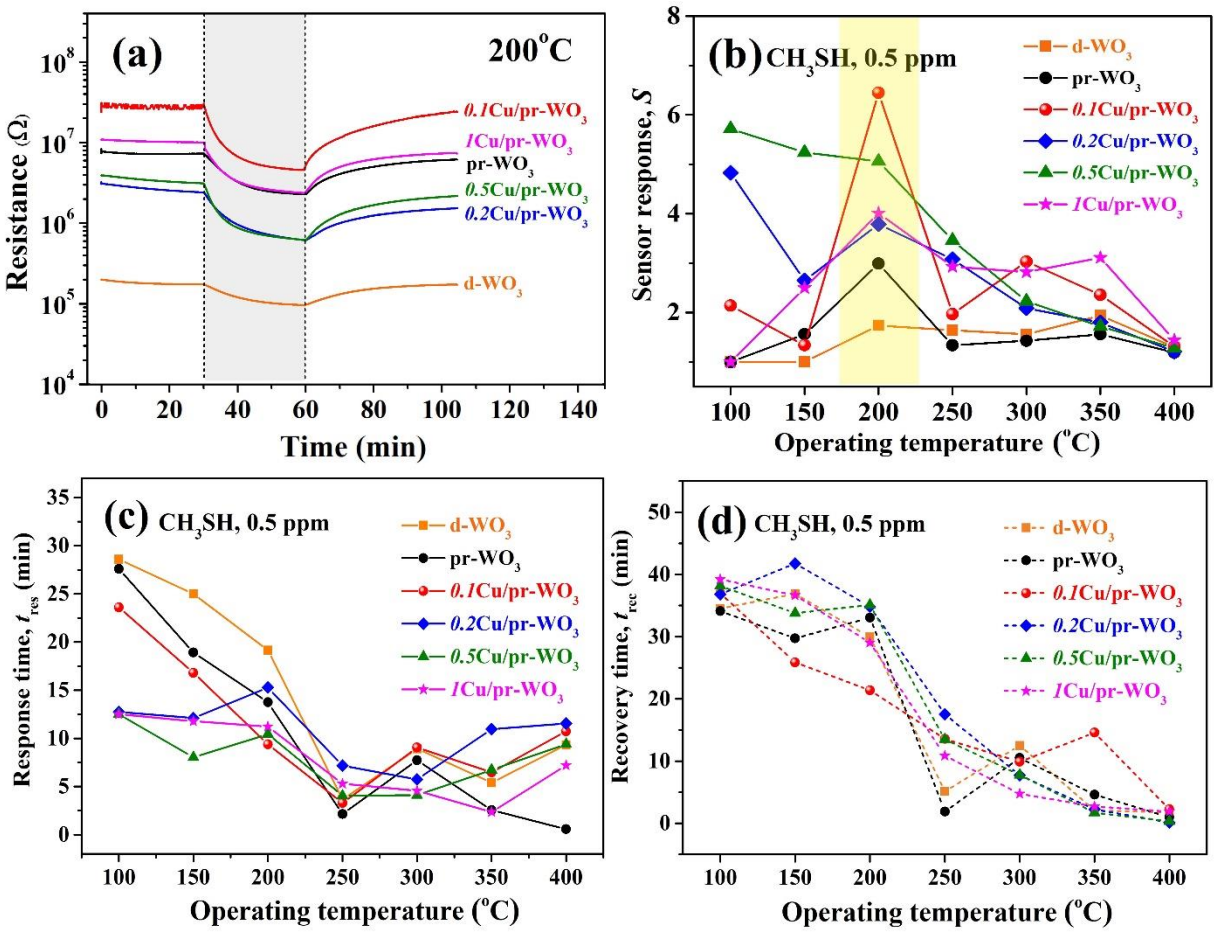

Figure 7. (a) Response transients of pr-WO_3 sensors with varying Cu contents and d-WO_3 sensor to 0.5 ppm CH_3SH at 200°C in air, (b) the CH_3SH response, (c) response time and (d) recovery time of these sensors versus operating temperature.

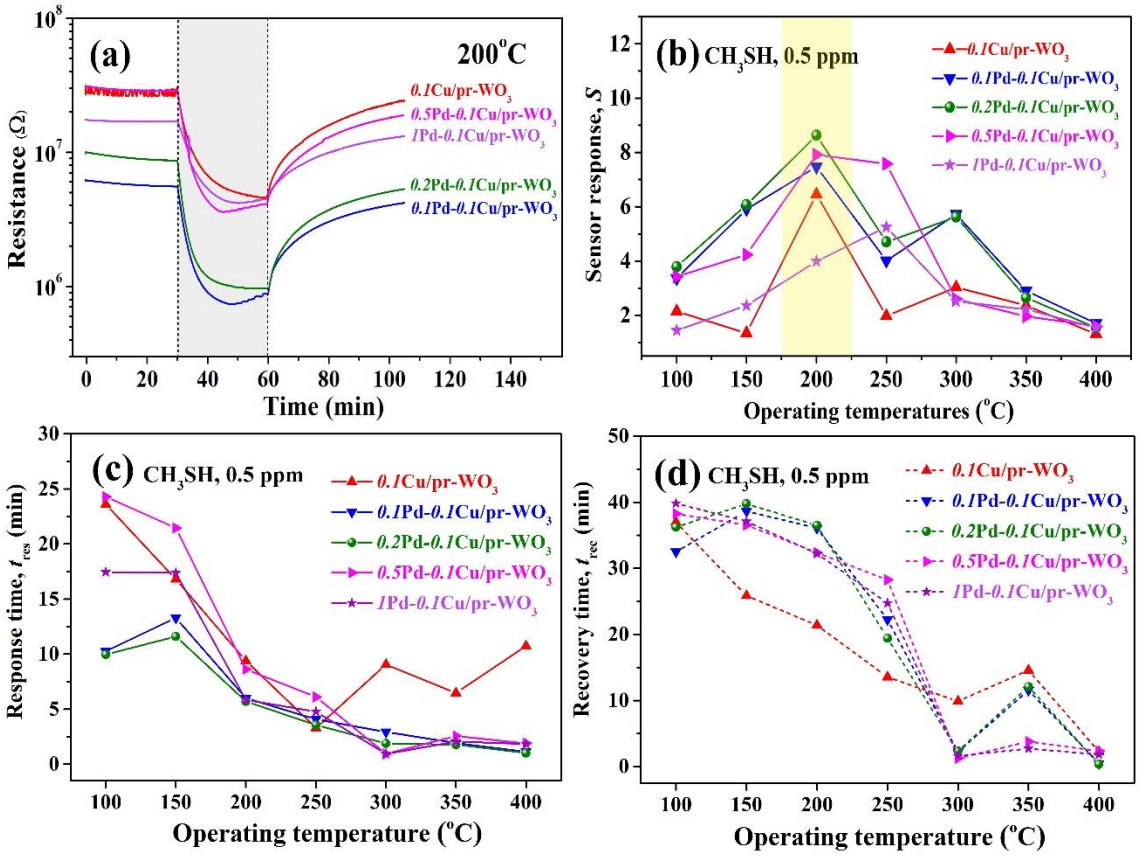

Figure 8. (a) Response transients of 0.1Cu/pr-WO_3 sensors with varying Pd co-loading contents to 0.5 ppm CH_3SH at 200°C in air, (b) the CH_3SH response, (c) response time and (d) recovery time of the sensors versus operating temperature.

The CH_3SH selectivity was investigated against 0.5 ppm H_2S, CH_3SCH_3, NO, NO_2, CH_4, C_2H_5OH and C_3H_6O at the optimal operating temperature of 200°C as illustrated in Fig. 9. It revealed that the single loading of CuO_x actually led to relatively high enhancement of H_2S response compared with that of CH_3SH response. In contrast, the responses to CH_3SCH_3, NO, NO_2, CH_4, C_2H_5OH and C_3H_6O were low and not evidently affected by the Cu content. Specifically, the *1*Cu/pr-WO_3 sensor exhibited the highest H_2S response and H_2S selectivity. With co-loading of 0.2 wt% Pd and 0.1 wt% Cu, CH_3SH of the *0.1*Cu/pr-WO_3 sensor increased moderately while the H_2S response decreased substantially and the responses to other gases

changed slightly, causing the sensor to become highly selective to CH_3SH. As the Pd content increased to 1 wt%, the CH_3SH response decreased more than the H_2S response did while those to other gases slightly decreased, resulting in relatively low CH_3SH selectivity against H_2S and other gases. The high selectivity with sufficiently high response at the low gas concentration attained via PdO_x co-loading could enable its practical use in targeted applications particularly the CH_3SH detection in breath for periodontal diagnoses.

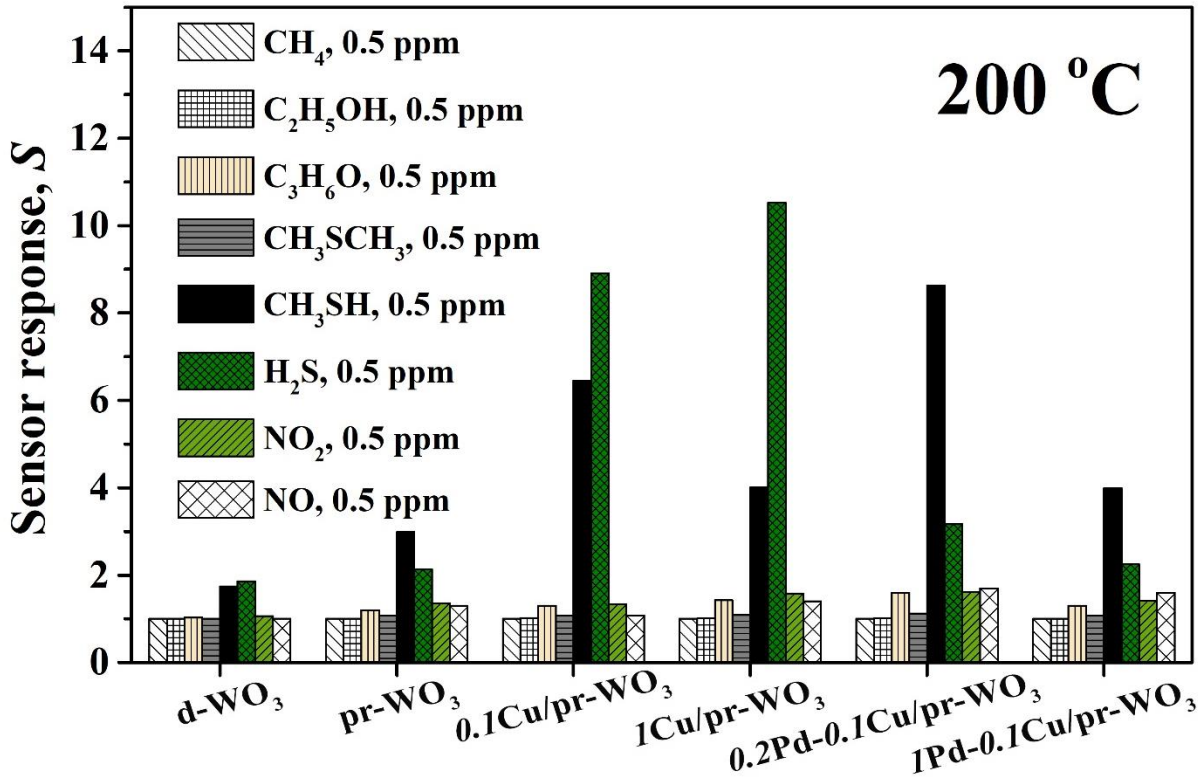

Figure 9. Responses of representative sensors to 0.5 ppm CH_3SH, H_2S, CH_3SCH_3, NO, NO_2, CH_4, C_2H_5OH and C_3H_6O at the optimal operating temperature of 200°C.

3.3. Sensing Mechanisms

The gas-sensing data demonstrated that the introduction of well-controlled macropores into WO_3 microspheres as well as the co-loading of PdO_x and CuO_x species on the pr-WO_3

microspheres were quite effective in improving the response and selectivity to CH_3SH against H_2S and several other breath gases. The formation of macropores in WO_3 microspheres understandably improved the gas diffusion from the top surface to the bottom part of the sensing layer and increased the effective gas interaction volume, leading to enhanced gas responses. Concerning the co-loading effects, the PdO_x and CuO_x loadings on the pr-WO_3 microspheres could further enhance the CH_3SH response via two fundamental mechanisms, namely electronic and chemical sensitizations as schematically described in Fig. 10. According to chemical-sensitization mechanisms, the CH_3SH response originates from the direct combustion of CH_3SH on the oxide surface through the positively charged adsorption of CH_3SH and/or the partially oxidized products.[9] Generally, CH_3SH would be oxidized at elevated temperatures and the partially oxidized product, dimethyldisulfide (CH_3SSCH_3), would be mainly produced at around 200°C according to the following reactions[21]:

$$CH_3SH + 3O_{ad}^- \rightarrow CO_2 + SO_2 + 2H_2O(g) + 3e^- \quad (1)$$

$$2CH_3SH + O_{ad}^- \rightarrow CH_3SSCH_3 + H_2O(g) + e^- \quad (2)$$

where O_{ad}^- represented negatively charged oxygen adsorbates on WO_3 surface. The complete oxidation of CH_3SH (eq. (1)) and the generation of CH_3SSCH_3 (eq. (2)) simultaneously occurred at some reactive sites on the surface of porous WO_3 as depicted in Fig. 10 (a). The number of oxygen adsorbates decreased by the reaction with CH_3SH while electrons were released back to porous WO_3 surface resulting in recession of depletion regions and a decrease of resistance. The enhanced reaction rate concerning CH_3SSCH_3 at 200°C could be a possible reason for the largest CH_3SH response of *pr*-WO_3 sensors at 200°C.

With loading of CuO_x at a moderately low content, CuO_x nanoparticles were dispersed on the porous WO_3 surfaces as depicted in Fig. 10(b). According to the XPS data, CuO_x mainly

comprised Cu_2O, which was a p-type semiconductor with the nominal energy gap (E_g) of 2.1 eV, work function (W) of 5.0 eV and electron affinity (χ) of 3.2 eV [25-26] while WO_3 was n-type with E_g = 2.7 eV, W = 4.9 eV and χ = 3.9 eV.[22, 27] Thus, CuO_x-WO_3 (p-n) heterojunctions would be formed through the structure and the small work function difference could induce thin extended depletion regions of electrons in the n-type WO_3 and holes in the p-type CuO_x as depicted in Fig. 11(a), leading to a small increase of electrical resistance in air. When subjected to CH_3SH, CuO_x could chemically catalyze the reactions (1)-(2) via the interaction with the active SH group, causing spillover reactions from CuO_x nanoparticles to WO_3. This provided more electrons, causing wider receded depletion regions, lower electrical resistance and higher CH_3SH response than the unloaded structure (electronic-sensitization effect).[28-29]

The co-loading process added nanoparticles of PdO_x containing mainly PdO, another p-type semiconductor (E_g = 2.5 eV, W = 3.7 eV and χ = 1.7 eV)[30-32], to the structure forming two kinds of heterojunctions: (1) p-n junctions of CuO_x-WO_3 and PdO_x-WO_3 and (2) p-p heterojunctions of CuO_x-PdO_x on the porous WO_3 surfaces. The hypothetical energy band analysis in Fig. 11(b) revealed that the behavior of PdO-WO_3 heterojunction was distinct from that of CuO_x-WO_3. After thermal stabilization of the PdO-WO_3 junctions, holes and electrons would be accumulated in PdO and WO_3 interfacial regions, resulting in receded depletion regions as depicted in Fig. 10(c) and a decrease of electrical resistance in accordance with the electrical data in Fig. 9(a). The electron accumulation in WO_3 at the interface could promote oxygen chemisorption, leading to the increase of O_{ad}^- concentration beneficial for the reducing reaction of CH_3SH (Eq. (1)-(2)). In addition, the excellent catalytic activity of PdO_x towards the sulfur functional group could further enhance the CH_3SH reactions at the PdO_x-WO_3 junctions leading to the enhanced CH_3SH response. As for the CuO_x-PdO_x (p-p) heterojunctions as

demonstrated in Fig. 11(c), the hole transfers between CuO_x and PdO_x led to hole accumulation in PdO_x and hole depletion in CuO_x causing changes in electrical behaviors to both catalyst.[33] This electronic interaction between PdO_x and CuO_x could further promote the CH_3SH interactions on WO_3 surfaces via electronic-sensitization effects as depicted in Fig. 10(c).

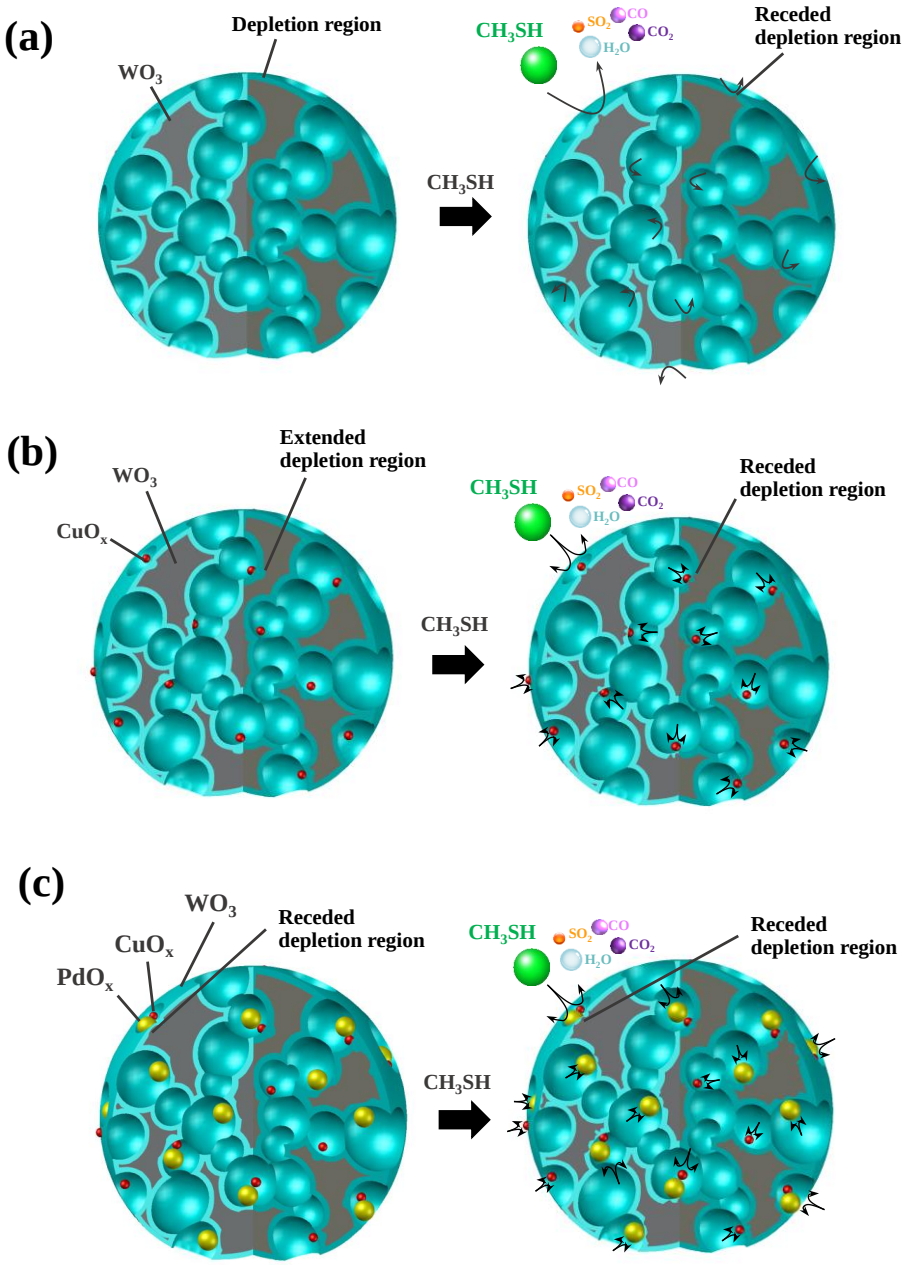

Figure 10. Schematic drawings of CH_3SH-sensing mechanisms for pr-WO_3 sensors with (a) no loading, (b) CuO_x loading, and (c) PdO_x-CuO_x co-loading.

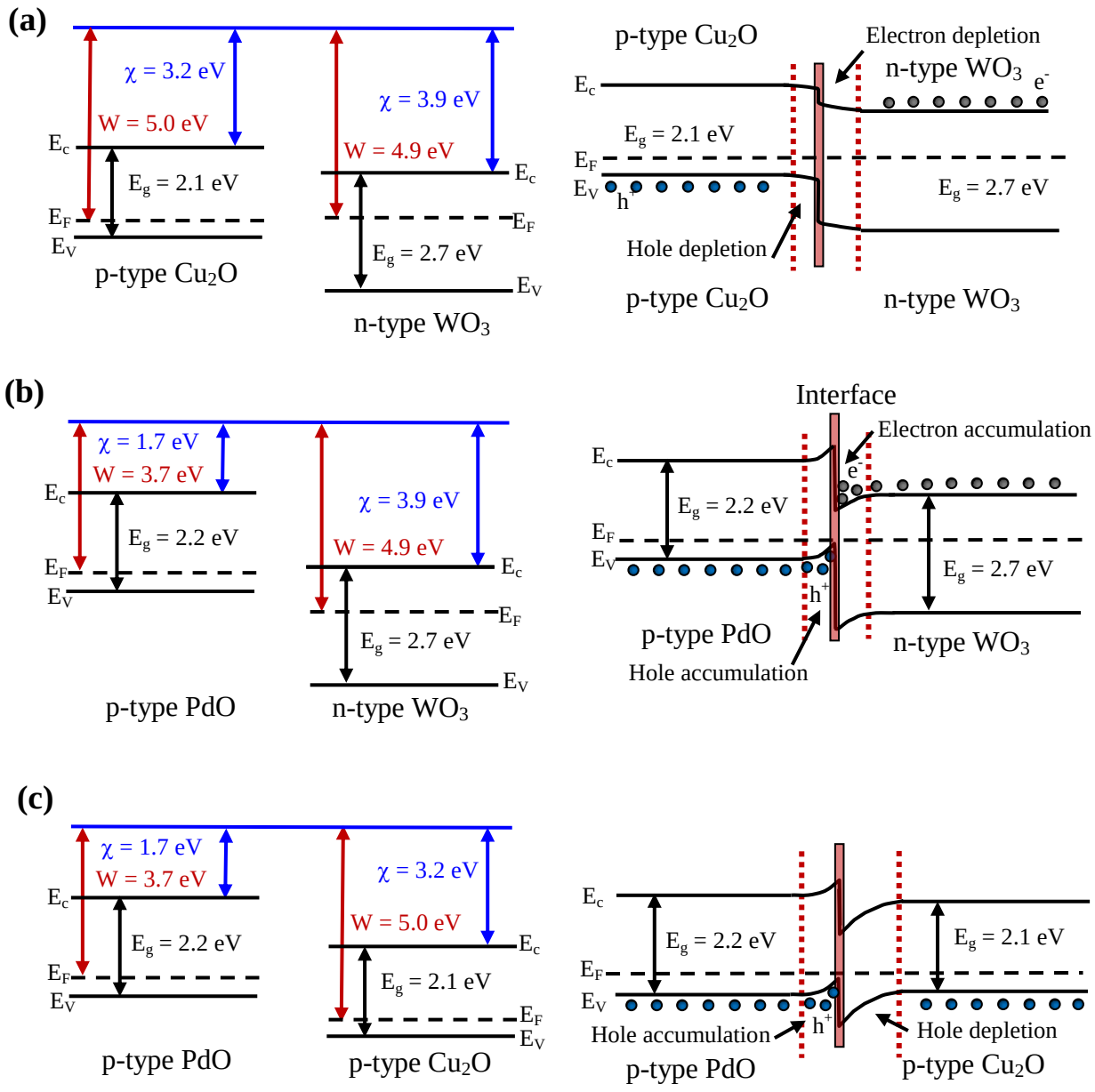

Figure 11. Energy band diagrams of (a) Cu_2O-WO_3, (b) PdO-WO_3 and (c) Cu_2O-PdO heterojunctions.

Distinctively, H_2S was relatively easily oxidized in comparison with CH_3SH since it would turn into SO_2 and H_2O with no partially oxidized product during the oxidation reaction. Thus, the H_2S response would largely depend on the combustion rate of H_2S especially in the

lower part of the sensing layer. With CuO_x loading, the H_2S oxidation would be catalytically enhanced, leading to a higher H_2S response. In addition, H_2S easily reacted with CuO_x to form CuS[34], augmenting the H_2S response especially at low temperatures. The co-loading of PdO_x with CuO_x could limit the H_2S oxidation in comparison with the single loading of CuO_x due possibly to the effect of lower electronic conductivity caused by hole depletion in CuO_x (Fig. 11 (c)). Moreover, the interaction between PdO_x and CuO_x could enhance the decomposition of CuS because of the large oxidation activity of more conductive PdO_x having accumulated holes (Fig. 11 (c)), which would reduce the formation of CuS from CuO and the H_2S response. Consequently, the *0.2*Pd-*0.1*Cu/pr-WO_3 sensor exhibited lower H_2S response and higher CH_3SH selectivity than the *0.1*Cu/pr-WO_3 sensor at a low temperature of 200°C. In the case of CH_3SCH_3, the CuO_x and PdO_x loadings could not catalyze its reducing reaction at a low temperature since fully oxidized CH_3SCH_3 molecules required a high dissociation energy. Concerning other gases including, NO, NO_2, CH_4, C_2H_5OH and C_3H_6O, the CuO_x and PdO_x catalysts were not effective for enhancing their adsorptions and reactions at low temperatures due partly to the absence of active sulfur functional groups.

4. CONCLUSIONS

In summary, PdO_x-CuO_x functionalized porous WO_3 microspheres were successfully synthesized via USP technique with PMMA microsphere templates for CH_3SH-sensing applications. From structural characterizations, ultra-small secondary nanostructures of CuO_x and PdO_x with mixed oxidation states (Cu^+/Cu^{2+} and Pd^0/Pd^{2+}) were formed and well dispersed on porous orthorhombic WO_3 microspheres with 100–600 nm in diameter. The gas-sensing results demonstrated that the formation of macropores in WO_3 microspheres by utilizing PMMA

microsphere templates and co-loading of PdO_x and CuO_x cooperatively enhanced the CH_3SH response, especially at a low optimal working temperature. Specifically, the porous WO_3 sensor with optimal Cu and Pd contents of 0.1 wt% and 0.2 wt% exhibited an optimal response of 8.6 to 0.5 ppm CH_3SH at 200°C. Moreover, the addition of PdO_x to CuO_x-loaded WO_3 sensors substantially improved the CH_3SH selectivity against H_2S and retained high selectivity against CH_3SCH_3, NO, NO_2, CH_4, C_2H_5OH and CH_3COCH_3. Therefore, the PdO_x-CuO_x functionalized porous WO_3 microspheres could be promising candidates for highly sensitive and selective CH_3SH detections in practical applications including biomedical and periodontal diagnoses.

AUTHOR INFORMATION

Corresponding Author

*C. Liewhiran. E-mail: cliewhiran@gmail.com.

Tel.: +66-81-408-2324 Fax: +66-53-943-440

ACKNOWLEDGMENTS

The authors gratefully acknowledge the financial support from the Royal Golden Jubilee Ph.D. Programme (RGJ) (PHD/0152/2559), the Mid-Career Research Grant, National Research Council of Thailand (NRCT). We also wish to thank Center of Excellence in Materials Science and Technology, Chiang Mai University for financial support under the administration of Materials Science Research Center, Faculty of Science, Chiang Mai University, National Research University (NRU) Project under the Office of the Higher Education Commission (CHE), Ministry of Education, Thailand, Graduate School, Materials Science Research Center, Department of Physics and Materials Science, Faculty of Science, Chiang Mai University. In

addition, the authors gratefully acknowledge the Thailand Research Fund for TRF Research Team Promotion Grant (RTA6180004). The special thanks should be given to Graduate School of Engineering, Nagasaki University, Japan, for the sensor facility and other technical assistance.

REFERENCES

(1) Lee, I.; Choi, S.-J.; Park, K.-M.; Lee, S. S.; Choi, S.; Kim, I.-D.; Park, C. O. The Stability, Sensitivity and Response Transients of ZnO, SnO_2 and WO_3 Sensors under Acetone. Toluene and H_2S Environments. Sens. Actuators B Chem. 2014, 197, 300-307.

(2) Van den Broek, A. M.; Feenstra, L.; de Baat, C. A Review of The Current Literature on Aetiology and Measurement Methods of Halitosis. J. Dent. 2007, 35 (8), 627-635.

(3) Nonaka, S.; Hyodo, T.; Shimizu, Y.; Egashira, M. Preparation of Macroporous Semiconductor Gas Sensors and Their Odur Sensing Properties. IEEJ Trans. SM 2008, 128 (4), 141-144.

(4) Shimizu, Y.; Kai, S.; Takao, Y.; Hyodo, T.; Egashira, M. Correlation Between Methylmercaptan Gas-Sensing Properties and its Surface Chemistry of SnO_2-Based Sensor Materials. Sens. Actuators B Chem. 2000, 65, 349-357.

(5) Poongodi, S.; Kumar, P. S.; Mangalaraj, D.; Ponpandian, N.; Meena, P.; Masuda, Y.; Lee, C. Electrodeposition of WO_3 Nanostructured Thin Films for Electrochromic and H_2S Gas Sensor Applications. J. Alloys Compd. 2017, 719, 71-81.

(6) Bolokang, A. S.; Motaung, D. E. Reduction-Oxidation of V_2O_5-WO_3 Nanostructured by Ball Milling and Annealing: Their Improved H_2S Gas Sensing Performance. Appl. Surf. Sci. 2019, 473, 164-173.

(7) Kabcum, S.; Channei, D.; Tuantranont, A.; Wisitsoraat, A.; Liewhiran, C.; Phanichphant, S. Ultra-Responsive Hydrogen Gas Sensors Based on PdO Nanoparticle-Decorated WO_3 Nanorods

Synthesized by Precipitation and Impregnation Methods. Sens. Actuators B Chem. 2016, 226, 76-89.

(8) Wu, C.-H.; Zhu, Z.; Huang, S.-Y.; Wu, R.-J. Preparation of Palladium-Doped Mesoporous WO_3 for Hydrogen Gas Sensors. J. Alloys Compd. 2019, 776, 965-973.

(9) Ueda, T.; Maeda, T.; Huang, Z.; Higuchi, K.; Izawa, K.; Kamada, K.; Hyodo, T.; Shimizu, Y. Enhancement of Methylmercaptan Sensing Response of WO_3 Semiconductor Gas Sensors by Gas Reactivity and Gas Diffusivity. Sens. Actuators B Chem. 2018, 273, 826-833.

(10) He, M.; Xie, L.; Zhao, X.; Hu, X.; Li, S.; Zhu, Z.-G. Highly Sensitive and Selective H_2S Gas Sensors Based on Flower-Like WO_3/CuO Composites Operating at Low/Room Temperature. J. Alloys Compd. 2019, 788, 36-43.

(11) Hyodo, T.; Fujii, E.; Ishida, K.; Ueda, T.; Shimizu, Y. Microstructural Control of Porous In_2O_3 Powders Prepared by Ultrasonic-Spray Pyrolysis Employing Self-Synthesized Polymethylmethacrylate Microspheres as a Template and Their NO_2-Sensing Properties. Sens. Actuators B Chem. 2017, 244, 992-1003.

(12) Ueda, T.; Ishida, K.; Kamada, K.; Hyodo, T.; Shimizu, Y. Improvement in NO_2 Sensing Properties of Semiconductor-Type Gas Sensors by Loading of Au Into Porous In_2O_3 Powders. Front. Mater. 2019, 1-10.

(13) Hyodo, T.; Nonaka, S.; Shimizu, Y.; Egashira, M. H_2S Sensing Properties and Mechanism of Macroporous Semiconductor Sensors. ECS Transactions 2008, 16, 317.

(14) Kukkola, J.; Mohl, M.; Leino, A.-R.; Mäklin, J.; Halonen, N.; Shchukarev, A.; Konya, Z.; Jantunen, H.; Kordas, K. Room Temperature Hydrogen Sensors Based on Metal Decorated WO_3 Nanowires. Sens. Actuators B Chem. 2013, 186, 90-95.

(15) Kim, S.; Park, S.; Park, S.; Lee, C. Acetone Sensing of Au and Pd-Decorated WO_3 Nanorod Sensors. Sens. Actuators B Chem. 2015, 209, 180-185.

(16) Yang, F.; Wang, F.; Guo, Z. Characteristics of Binary WO_3@CuO And Ternary WO_3@PDA@CuO Based on Impressive Sensing Acetone Odor. J. Colloid. Interface. Sci. 2018, 524, 32-41.

(17) Aregahegn, A.; Gedamu, A.; Chen, H.-M.; Berhe, T.; su, w.-n.; Hwang, B. J. Highly Stable Cus and CuS-Pt Catalyzed Cu_2O/CuO Heterostructure as Efficient Photocathode for Hydrogen Evolution Reaction. J. Mater. Chem. A 2015, 4.

(18) Karthik, T. V. K.; Olvera, M. d. l. L.; Maldonado, A.; Gómez Pozos, H. CO Gas Sensing Properties of Pure and Cu-Incorporated SnO_2 Nanoparticles: A Study of Cu-Induced Modifications. Sensors (Basel) 2016, 16 (8), 1283.

(19) Sánchez-Martínez, D.; Martínez-de la Cruz, A.; López-Cuéllar, E. Synthesis of WO_3 Nanoparticles by Citric Acid-Assisted Precipitation and Evaluation of Their Photocatalytic Properties. Mater. Res. Bull. 2013, 48 (2), 691-697.

(20) Sunding, M. F.; Hadidi, K.; Diplas, S.; Løvvik, O. M.; Norby, T. E.; Gunnæs, A. E. XPS Characterization of In Situ Treated Lanthanum Oxide and Hydroxide Using Tailored Charge Referencing and Peak Fitting Procedures. J. Electron Spectrosc. Relat. Phenom. 2011, 184 (7), 399-409.

(21) Kaur, J.; Anand, K.; Kohli, N.; Kaur, A.; Singh, R. C. Temperature Dependent Selective Detection of Hydrogen and Acetone using Pd Doped WO_3/Reduced Graphene Oxide Nanocomposite. Chem. Phys. Lett. 2018, 701, 115-125.

(22) Zhang, J.; Zhang, L.; Leng, D.; Ma, F.; Zhang, Z.; Zhang, Y.; Wang, W.; Liang, Q.; Gao, J.; Lu, H. Nanoscale Pd Catalysts Decorated WO_3–SnO_2 Heterojunction Nanotubes for Highly Sensitive and Selective Acetone Sensing. Sens. Actuators B Chem. 2020, 306, 127575.

(23) Sotomayor, F.; Cychosz, K.; Thommes, M. Characterization of Micro/Mesoporous Materials by Physisorption: Concepts and Case Studies. Acc. Mater. Surf. Res. 2018, 3 (2), 34-50.

(24) Garcia, D.; Picasso, G.; Hidalgo, P.; Peres, H. E. M.; Sun Kou, R.; Gonçalves, J. M. Sensors Based on Ag-Loaded Hematite (α-Fe_2O_3) Nanoparticles for Methyl Mercaptan Detection at Room Temperature. Anal. Chem. Res. 2017, 12, 74-81.

(25) Deuermeier, J.; Liu, H.; Rapenne, L.; Calmeiro, T.; Renou, G.; Martins, R.; Muñoz-Rojas, D.; Fortunato, E. Visualization of Nanocrystalline CuO In the Grain Boundaries of Cu_2O Thin Films and Effect on Band Bending and Film Resistivity. APL Mater. 2018, 6 (9), 096103.

(26) Brandt, R. E.; Young, M.; Park, H. H.; Dameron, A.; Chua, D.; Lee, Y. S.; Teeter, G.; Gordon, R. G.; Buonassisi, T. Band Offsets of N-Type Electron-Selective Contacts on Cuprous Oxide (Cu_2O) for Photovoltaics. Appl. Phys. Lett. 2014, 105 (26), 263901.

(27) Lim, S.-H.; Kim, H.-K. Deposition Rate Effect on Optical and Electrical Properties of Thermally Evaporated WO_{3-x}/Ag/WO_{3-x} Multilayer Electrode for Transparent and Flexible Thin Film Heaters. Sci. Rep. 2020, 10 (1), 8357.

(28) Ji, H.; Zeng, W.; Li, Y. Gas Sensing Mechanisms of Metal Oxide Semiconductors: A Focus Review. Nanoscale 2019, 11 (47), 22664-22684.

(29) Liu, B.; Cai, D.; Liu, Y.; Wang, D.; Wang, L.; Wang, Y.; Li, H.; Li, Q.; Wang, T. Improved Room-Temperature Hydrogen Sensing Performance of Directly Formed Pd/WO_3 Nanocomposite. Sens. Actuators B Chem. 2014, 193, 28-34.

(30) Ramond, T. M.; Davico, G. E.; Hellberg, F.; Svedberg, F.; Salén, P.; Söderqvist, P.; Lineberger, W. C. Photoelectron Spectroscopy of Nickel, Palladium, and Platinum Oxide Anions. J. Mol. Spectrosc. 2002, 216 (1), 1-14.

(31) Ryabtsev, S.; Shaposhnik, A.; Samoylov, A.; Sinelnikov, A.; Soldatenko, S.; Kushchev, S.; Ievlev, V. Thin Films of Palladium Oxide for Gas Sensors. Dokl. Phys. Chem. 2016, 470, 158-161.

(32) Rogal, J.; Reuter, K.; Scheffler, M. Thermodynamic Stability of PdO Surfaces. Phys. Rev. B 2004, 69 (7), 075421.

(33) Hu, X.; Zhu, Z.; Chen, C.; Wen, T.; Zhao, X.; Xie, L. Highly Sensitive H_2S Gas Sensors Based on Pd-Doped CuO Nanoflowers with Low Operating Temperature. Sens. Actuators B Chem. 2017, 253, 809-817.

(34) Maekawa, T.; Tamaki, J.; Miura, N.; Yamazoe, N. Improvement of Copper Oxide–Tin Oxide Sensor for Dilute Hydrogen Sulfide. J. Mater. Chem. 1994, 4 (8), 1259-1262.